Materials Science and Engineering C 75 (2017) 1049–1058

Contents lists available at ScienceDirect

Materials Science and Engineering C

journal homepage: www.elsevier.com/locate/msec

Antibacterial, osteogenic, and angiogenic activities of $SrTiO_3$ nanotubes embedded with Ag_2O nanoparticles

Yi Chen [a], Ang Gao [b], Long Bai [a], Yueyue Wang [a], Xin Wang [a], Xiangyu Zhang [a], Xiaobo Huang [a], Ruiqiang Hang [a,*], Bin Tang [a], Paul K. Chu [b,*]

[a] Research Institute of Surface Engineering, Taiyuan University of Technology, Taiyuan 030024, China
[b] Department of Physics and Materials Science, City University of Hong Kong, Tat Chee Avenue, Kowloon, Hong Kong, China

ARTICLE INFO

Article history:
Received 23 January 2017
Received in revised form 27 February 2017
Accepted 2 March 2017
Available online 06 March 2017

Keywords:
TiO_2 nanotubes
Strontium
Silver
Bacterial resistance
Angiogenesis
Osteogenesis

ABSTRACT

Biomedical titanium (Ti) implants with good anti-infective, osteogenic, and angiogenic properties are in great demand. $SrTiO_3$ nanotubes (NTs) are embedded with silver oxide (Ag_2O) nanoparticles (NPs) (denoted as NT-Sr-Ag) by a hydrothermal treatment of TiO_2 NTs containing Ag_2O NPs (denoted as NT-Ag) in a $Sr(OH)_2$ solution. The morphology, composition, microstructure, ion release phenomenon, as well as antibacterial, osteogenic, and angiogenic activities are investigated in details. During the hydrothermal treatment, the amorphous TiO_2 in the NTs morphs into cubic $SrTiO_3$ gradually and the ordered nanotubular architecture is preserved. Some Ag_2O NPs are incorporated into the structure although some of them dissolve in the solution. Long-term bacterial resistance against *Staphylococcus aureus* is observed as a result of the prolonged and controllable Ag^+ release. NT-Sr-Ag can also release Sr^{2+} similarly to stimulate osteoblasts to secrete the vascular endothelial growth factor (VEGF). Both the released Sr^{2+} and secreted VEGF upregulate the alkaline phosphatase (ALP) activity and extracellular matrix mineralization of osteoblasts. Furthermore, better angiogenic activity is observed when endothelial cells are cultured in NT-Sr-Ag conditioned media when compared with that in NT-Ag conditioned media, which is believed to be ascribed to the positive regulation of VEGF secretion of Sr^{2+}. NT-2Sr-Ag and NT-3Sr-Ag (Hydrothermal treatment for 2 and 3 h, respectively) exhibit excellent antibacterial, osteogenic, and angiogenic activities and are promising in biomedical implants.

1. Introduction

Although hard tissue implants made of titanium (Ti) and its alloys are widely used clinically [1–3], there are still concerns about prosthetic loosening and post-operative infection [4–7]. Various surface modification techniques have been utilized to alleviate these problems [8–10]. Recently, titanium dioxide nanotubes (denoted as NT-TiO_2) prepared by anodization have been extensively researched [11,12]. The diameter of the NT-TiO_2 can be easily adjusted by varying the anodization parameters and these tunable nanoscale morphologies can serve as cues to direct cell and tissue response to facilitate osseointegration [13–15]. Moreover, the tubular geometry is a good platform for targeted delivery of functional agents [16] such as the nutrient elements like Sr, Si, and Zn [17–21] as well as antibacterial elements like Ag and Cu [22–26]. For example, in our previous work, Ag was incorporated into NT-TiO_2 to produce long-term antibacterial activity without showing negative effects on the cytocompatibility and osteoblast functions [22].

Sr has aroused clinical interests due to its dual effects of improved bone formation and inhibition of bone resorption [27,28]. Sr^{2+} increases osteoblast replication, differentiation, and bone matrix mineralization *via* a calcium sensing receptor (CaR) dependent mechanism [28–31]. Sr loaded nanotubular structures (NT-Sr) have been fabricated by a hydrothermal treatment (HT) of NT-TiO_2 in the $Sr(OH)_2$ solution [19]. Long-lasting and controllable Sr^{2+} release has been observed and the optimal Sr^{2+} release leading to favorable osteogenic properties. At the same time, angiogenesis is crucial to bone healing and regeneration in order to restore the blood supply [32]. Better angiogenesis around the implant promotes the tissue integration and improves the anti-infection ability by triggering the host defense [33–35]. In addition, Sr^{2+} has been shown to stimulate osteoblasts to secrete the vascular endothelial

* Corresponding authors.
E-mail addresses: hangruiqiang@tyut.edu.cn (R. Hang), paul.chu@cityu.edu.hk (P.K. Chu).

http://dx.doi.org/10.1016/j.msec.2017.03.014
0928-4931/

growth factor (VEGF) [36,37] which plays dual roles in the osteogenic and angiogenic activities [38–40]. In this study, Ag and Sr are incorporated into NT-TiO_2 (denoted as NT-Sr-Ag) to endow the materials with good antibacterial, osteogenic, and angiogenic activities.

2. Materials and methods

2.1. Deposition of TiAg coatings by magnetron sputtering

The Ti foils (99.7% purity) were cut into pieces with dimensions of 10 mm × 10 mm × 0.3 mm as substrates. Before deposition, they were ultrasonically cleaned with acetone, ethanol, and deionized water sequentially followed by drying in air. The TiAg coatings were deposited on the Ti foils by pulsed direct current (DC) magnetron sputtering with TiAg targets. A high purity Ti target was used as control. Prior to deposition, both the substrates and TiAg targets were sputter-cleaned for 30 min at a bias of −800 V, duty factor of 40%, pulse frequency of 60 kHz, and pressure of 5.0 Pa. Deposition of the TiAg and pure Ti coatings was conducted for 3 h at a target power of 300 W, working pressure of 0.8 Pa, substrate bias of −80 V, pulse frequency of 60 kHz, and duty factor of 60%.

2.2. Preparation of NT-Ag

NT-Ag was fabricated by anodization of the TiAg coatings in an ethylene glycol electrolyte containing 0.3 wt% NH_4F and 2.0 vol% H_2O at 30 V for 4 h. Anodization was carried out with a conventional two-electrode configuration. The Ti foil with the coating was the anode and a graphite rod was the cathode. Afterward anodization, the samples were ultrasonically cleaned in deionized water for 1 min to remove the electrolyte as well as undesirable irregular surface oxide.

2.3. Preparation of NT-Sr-Ag

Sr was incorporated into the NT-Ag hydrothermally. Briefly, the NT-Ag samples were placed in 33.5 mL of 0.02 M $Sr(OH)_2$ in a 50 mL Teflon-lined autoclave and heated at 200 °C for 1, 2, 3, and 5 h (samples were denoted as NT-1Sr-Ag, NT-2Sr-Ag, NT-3Sr-Ag, and NT-5Sr-Ag, respectively). The specimens were then ultrasonically washed with 1 M HCl for 5 min and deionized water for 1 min followed by drying in air.

2.4. Sample characterization

The surface and cross-sectional morphologies of the samples were observed by field-emission scanning electron microscopy (FE-SEM, JSM-7001F, JEOL, Japan) at 10 kV. The cross-sectional images were taken from the fragments of the NTs after scraping the samples with a sharp metallic tip. The distribution of Ti, O, Sr, and Ag along the longitudinal direction of the NTs was determined by energy-dispersive X-ray spectroscopy (EDS, QX200, Bruker, Germany). X-ray photoelectron spectroscopy (XPS, K-Alpha, Thermo, America) with monochromatic Al K_α radiation was conducted to determine the surface elemental compositions and chemical states. The crystal structure was determined by X-ray diffraction (XRD, DX-2700, Haoyuan, China). The atomic-scale microstructure of NT-Ag and NT-Sr-Ag was characterized by high-resolution transmission electron microscopy (HR-TEM, Tecnai G2 F20 S-Twin, FEI, America) at an accelerating voltage of 200 kV and selected-area electron diffraction (SAED). Prior to TEM examination, the samples were bent repeatedly to delaminate the NTs from the substrate and the samples were dispersed in alcohol ultrasonically and mounted onto grids.

2.5. Sr and Ag release

NT-Ag and NT-Sr-Ag were immersed in 5 mL of phosphate buffered solution (PBS) at 37 ± 0.5 °C and the solution was refreshed daily. The process was repeated for 60 days. The PBS containing released Sr^{2+} and Ag^{+} were collected at time points of 1, 10, 30, and 60 days and analyzed by inductively-coupled plasma mass spectroscopy (ICP-MS, Agilent 7500, Agilent, America).

2.6. Antibacterial assay

The antibacterial properties of NT-Ag and NT-Sr-Ag against gram-positive *Staphylococcus aureus* (*S. aureus*, ATCC6538) were assessed by plate-counting method. The samples in each group were immersed in 5 mL of PBS (refreshed daily) for 1, 10, 30, and 60 days. At each time point, the samples were collected for antibacterial assay. The bacteria were cultured in beef extract-peptone (BEP, Sangon, China) under agitation for 18 h at 37 ± 0.5 °C. Afterwards, 50 μL of the bacterial suspension diluted with PBS to a concentration of 1.0×10^5 CFU/mL were introduced onto each sample and incubated at 37 ± 0.5 °C for 12 h in darkness. At the end of the incubation period, each sample was rinsed in 2 mL of PBS and the viable bacteria in the PBS were quantified by standard serial dilution and plate-counting. Three samples in each group were tested at each time point and the antibacterial rate was calculated by the following equation: $R = (B - A) / B \times 100\%$, where R is the antibacterial rate, B represents the average number of colony-forming units (CFU) on the NT-TiO_2 (negative control), and A is the average number of CFU on the NT-Ag and NT-Sr-Ag.

2.7. Cell culture

The newborn mouse calvaria-derived MC3T3-E1 subclone 14 pre-osteoblasts (osteoblasts) and human endothelial cell line EA.hy926 (ECs) were provided by the Shanghai cell bank of the Chinese Academy of Sciences and maintained as recommended by the supplier. The osteoblasts and ECs were cultured in α-MEM (Gibco, America) and high-glucose DMEM (Gibco, America), respectively, supplemented with 10% fetal bovine serum (FBS, Sijiqing, China) and 1% antibiotic-antimycotic solution (100 units/mL penicillin (Weifang Pharmaceutical, China), 100 mg/mL streptomycin (Lukang Pharmaceutical, China), and 0.25 μg/mL amphotericin B (Sangon, China)). The cells were seeded on the sample surfaces on a 24-well culture plate at a density of 2×10^4 cells/cm^2 unless otherwise specified. In the alkaline phosphatase (ALP) activity, collagen secretion, and extracellular matrix mineralization experiments, after the osteoblasts were cultured in the normal medium for 3 days, 10 mM β-glycerophosphate (Ekear, China), 50 μg/mL ascorbic acid (Ekear, China), and 10 nM dexamethasone (Ekear, China) were added to the medium to induce osteogenic differentiation.

2.8. Cell adhesion and cytoskeleton assembly

After the osteoblasts were seeded and incubated for 0.5, 1, and 4 h, the samples were rinsed thrice in PBS to remove nonadherent cells and the adherent cells were fixed with 4% paraformaldehyde (PFA, Damao, China) for 30 min and stained with 4, 6-diamidino-2-phenylindole (DAPI, Sigma, America) for 10 min. The quantity of adherent cells were determined by counting six random fields under 100 × magnification under a confocal laser scanning microscope (CLSM, C2 Plus, Nikon, Japan). The cytoskeleton organization of the osteoblasts after incubation for 1, 4, and 24 h were observed by CLSM after fixing with 4% PFA for 30 min and staining with FITC-Phalloidin (Sigma, America) for 40 min.

2.9. Cell viability

The viability of the osteoblasts cultured on the samples for 1, 3, and 5 days was determined by Live/Dead (Invitrogen, America) staining and MTT (Sigma, America) assay according to the manufacturer's instruction. With regard to the MTT assay, at each

time point, the samples were rinsed thrice with PBS and transferred to a new 24-well plate. Afterwards, 100 μL of the MTT solution and 900 μL of the fresh culture medium were added to each well and incubated at 37 °C for 4 h to form formazan that was dissolved in dimethyl sulfoxide (DMSO, Sangon, China). The optical density (OD) of each solution was measured at 490 nm on a microplate reader (Infinite F50, TECAN, Switzerland).

2.10. ALP activity

After the osteoblasts were seeded on the samples, cultured for 3 days, and underwent osteogenic induction for 3 and 7 days, they were fixed with 4% PFA and stained with BCIP/NBT ALP Color Development Kit (Beyotime, China) to qualitatively evaluate the ALP activity. In the quantitative assay, the cells were lysed in 0.5 mL of distilled water

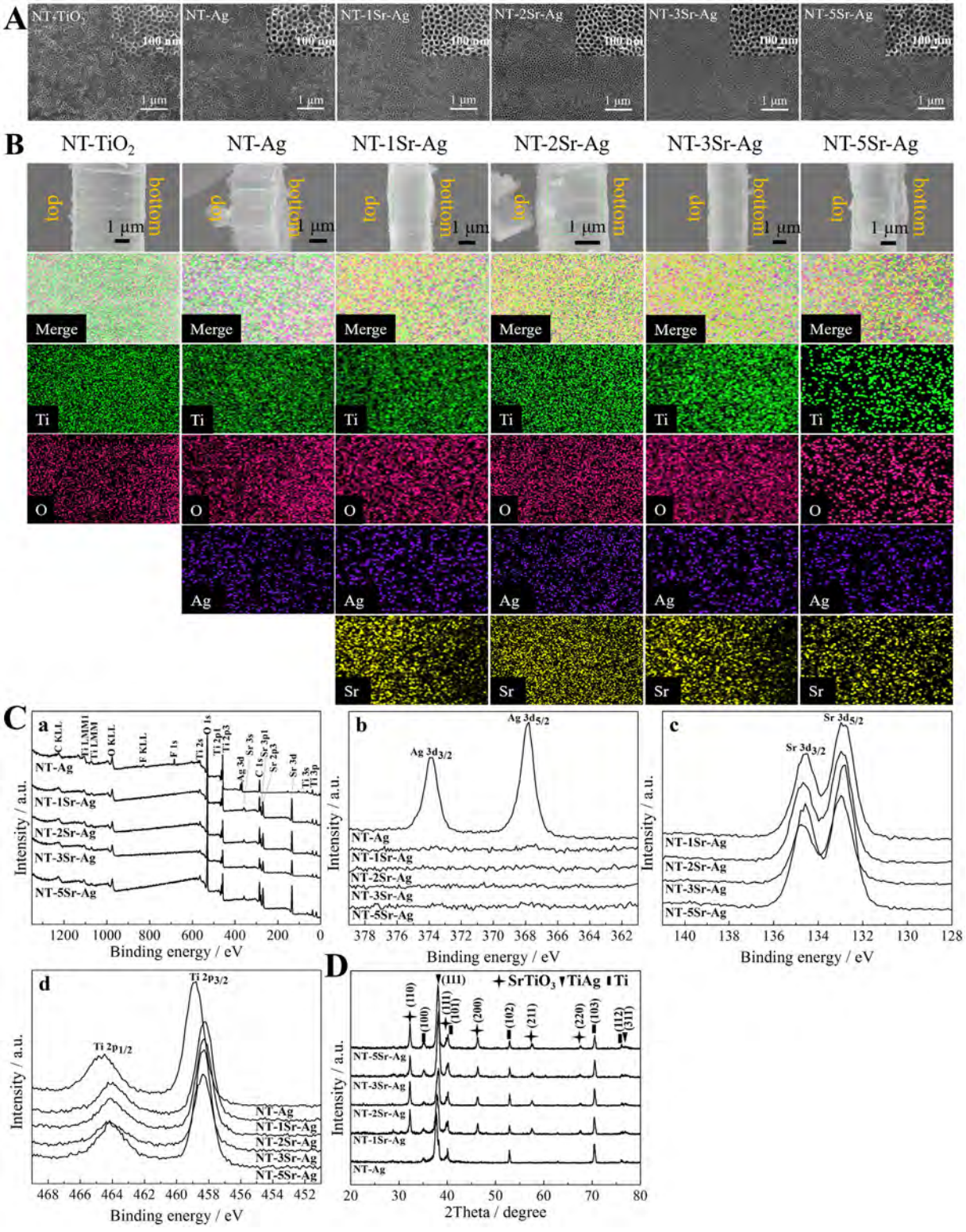

Fig. 1. (A) Surface SEM images of NT-TiO_2, NT-Ag, and NT-Sr-Ags. The inset in each image shows the respective high-magnification morphology; (B) Cross-sectional SEM images of the samples and corresponding elemental maps; (C) XPS survey spectra (a) and high-resolution spectra of Ag 3d (b), Sr 3d (c), and Ti 2p (d); (D) XRD spectra of the samples.

Table 1
Surface elemental concentrations of NT-Ag and NT-Sr-Ag determined by XPS.

Samples	Atomic concentration (at.%)						
	Sr	Ag	Ti	O	C	N	F
NT-Ag	–	0.75	11.87	37.5	40.58	3.67	5.62
NT-1Sr-Ag	12.46	0.18	10.16	37.25	36.39	2.53	1.03
NT-2Sr-Ag	12.5	0.18	10.35	37.04	37.14	1.18	1.61
NT-3Sr-Ag	12.47	0.16	10.63	38.64	33.75	2.6	1.74
NT-5Sr-Ag	12.48	0.15	9.68	38.65	35.42	2.67	0.96

through four standard freeze-thaw cycles. The lysate mixed with the solution of the alkaline phosphatase assay kit (Beyotime, China) was incubated at 37 °C for 30 min. The ALP activity levels were evaluated colorimetrically and normalized to the total protein content determined by the bicinchoninic acid (BCA) protein assay kit (Beyotime, China).

2.11. Collagen secretion

Secretion of type I collagen by the osteoblasts was assessed by the direct red 80 staining method. After osteogenic induction for 7 and 14 days, the cells cultured on sample surfaces were fixed in 4% PFA and stained with 0.1% Direct Red 80 (Sigma, America) in aqueous saturated picric acid for 18 h. After thorough rinsing with 0.1 M acetic acid to remove the unbound stain, the stained samples were photographed on a metallographic microscope (Axiovert 25, Zeiss, Germany). In the quantitative assessment, the stain on each sample surface was eluted with 1 mL of the fading solution (0.2 M NaOH/methanol 1:1) for 30 min and the optical density at 570 nm was measured on the microplate reader.

2.12. Extracellular matrix mineralization

Extracellular matrix mineralization by the osteoblasts was evaluated by Alizarin Red S (Sigma, America) staining. After osteogenic induction for 14 and 21 days, the cells on the samples were fixed with 75% ethanol for 1 h and stained in 40 mM Alizarin Red S for 30 min at room temperature. The excessive stain was removed by rinsing with distilled water repeatedly and images were acquired on the metallographic microscope. Quantitative analysis was performed by eluting the absorbed stain with 500 μL of 10% cetylpyridinium chloride (Sinopharm, China) in 10 mM sodium phosphate (Sinopharm, China) (pH 7.0) for 2 h and the optical density at 570 nm was measured on the microplate reader.

2.13. VEGF secretion

After the osteoblasts were seeded on the samples in 1 mL of the culture medium and cultured for 48 h, the supernatants of the culture medium (denoted as SCM) were collected and VEGF concentrations in them were measured by VEGF ELISA kit (R&D Systems, America) according to the manufacturer's specification.

2.14. NO production

A NO fluorescence probe, 4-Amino-5-Methylamino-2′,7′-Difluorofluorescein Diacetate (DAF-FM DA, Beyotime, China), was used to evaluate the influence of the SCM on NO production by ECs. The cells were seeded on a 24-well plate and cultured in 0.5 mL of SCM and 0.5 mL of complete culture medium on each well. After culturing for 24 h, each sample was rinsed thrice with PBS and incubated with 50 μL of 5 mM DAF-FM DA for 20 min at 37 °C in darkness. After incubation, each sample was rinsed thrice with PBS and examined by CLSM. The mean fluorescence intensity (MFI) for each sample was calculated using the ImageJ 1.45 software (NIH, America).

2.15. In vitro angiogenesis

The *in vitro* angiogenesis assay was conducted using ECMatrix™ (Millipore, Cat. No. ECM625, America). The ECMatrix gel was thawed at 4 °C overnight, mixed with the ECMatrix diluent buffer, placed on a 96-well plate, and incubated at 37 °C for 1 h. The ECs were seeded on the ECMatrix gel at the density of 2×10^4 cells per well with the SCM from different samples and then incubated at 37 °C for 4, 8, and 18 h. At each time point, the cells from at least three random fields were at 100× magnification using an inverted light microscope (BM-37XB, BM, China).

2.16. Statistical analysis

The data were collected from three separate experiments and expressed as mean ± standard deviation. The statistical analysis was performed by the software SPSS 14.0 software (IBM, America). The statistical significance among groups was calculated by one-way ANOVA followed by the Student-Newman-Keuls test. The difference was considered to be significant and highly significant when the p values were less than 0.05 and 0.01, respectively.

3. Results

3.1. Sample synthesis and characterization

Ag in the form of Ag_2O NPs was *in situ* incorporated into NT-TiO_2 by anodization of the deposited TiAg coatings. NT-Ag underwent HT in Sr-containing solutions for 1, 2, 3, and 5 h to load Sr into NT-Ag to generate NT-Sr-Ag. The morphology of the samples by FE-SEM is shown in Fig. 1A revealing uniform NTs. Anodization of the deposited TiAg coatings under optimal condition produces a well-defined nanotubular structure (NT-Ag) which is preserved after HT. The insets in Fig. 1A indicate that the diameter of NTs in NT-TiO_2 and NT-Ag is about 80 nm with a wall thickness of about 10 nm, although that of NT-Sr-Ag decreases slightly with HT time. The cross-sectional images in Fig. 1B indicate that the length of NT-TiO_2 is about 6 μm but that of NT-Ag drops to 3 μm due to the incorporation of Ag. The HT has little influence on the tubular length as NT-Sr-Ag has the same length as NT-Ag irrespective of the reaction time. The elemental maps along the longitudinal direction of the NTs disclose even distributions of Ti, O, and Ag along the entire length of the NTs while the Sr concentration decreases with depth gradually (Fig. 1B).

The elemental composition and chemical states of NT-Ag and NT-Sr-Ag are determined by XPS and the surface atomic concentrations are listed in Table 1. Ti, O, C, N, F, and Ag are detected from NT-Ag and additional Sr is found from NT-Sr-Ag. C, N, and F come from surface contamination and the organic fluoride-containing electrolyte. Fig. 1C shows the survey spectra and high-resolution spectra of Ag 3d, Sr 3d, and Ti 2p. The Ag $3d_{5/2}$ peak at 367.7 eV in Fig. 1Cb from NT-Ag corresponds to the binding energy of Ag^+, indicating that Ag exists mainly in the oxidized state in NT-Ag [22]. The absence of these peaks for NT-Sr-Ag indicates a Ag concentration that is below the detect limit of XPS. The fine XPS spectra of Sr 3d of NT-Sr-Ag in Fig. 1Cc can be deconvoluted into Sr $3d_{5/2}$ and Sr $3d_{3/2}$ located at 132.9 eV and 134.6 eV, respectively, in accordance with those reported for $SrTiO_3$ [41]. The high-resolution spectra of Ti 2p (Fig. 1Cd) obtained from NT-Ag show two peaks at 458.3 eV and 463.9 eV and two peaks at 458.8 eV and 464.6 eV are detected from NT-Sr-Ag, indicating the presence of TiO_2 in the NT-Ag and $SrTiO_3$ in NT-Sr-Ag [42].

The structure and crystal phase of NT-Ag and NT-Sr-Ag are analyzed by XRD as shown in Fig. 1D. Owing to the amorphous nature of the as-anodized TiO_2 NTs, only Ti and TiAg but no peaks from TiO_2 are detected from NT-Ag. After HT in the $Sr(OH)_2$ solution, additional diffraction peaks from cubic crystalline $SrTiO_3$ emerge. These $SrTiO_3$ peaks become more intense with HT time and the two intense peaks at 32.4° and 39.9°

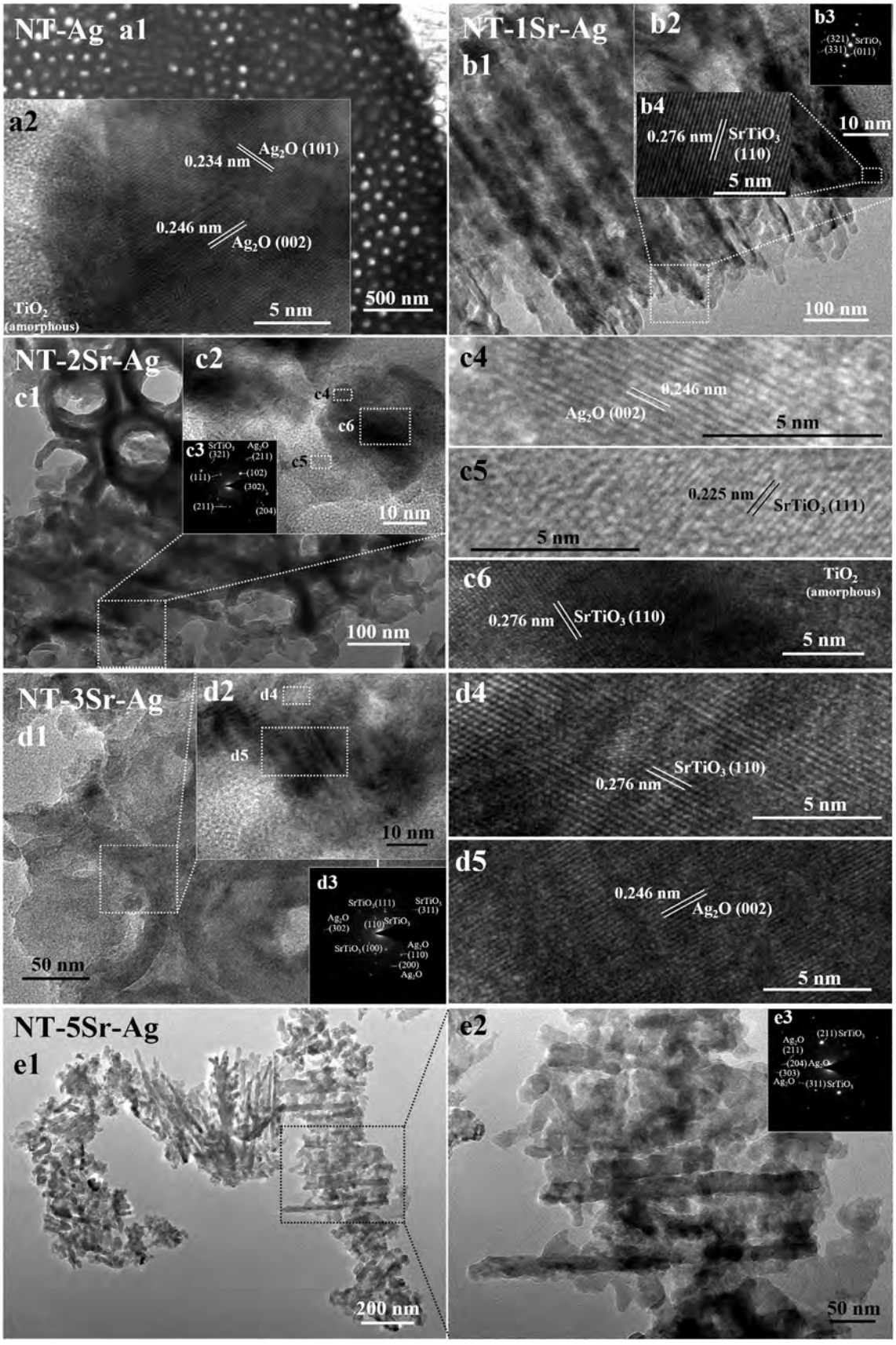

Fig. 2. TEM images and SAED patterns of (a) NT-Ag, (b) NT-1Sr-Ag, (c) NT-2Sr-Ag, (d) NT-3Sr-Ag, and (e) NT-5Sr-Ag and the corresponding high-magnification or HR-TEM images of the area enclosed by the rectangle.

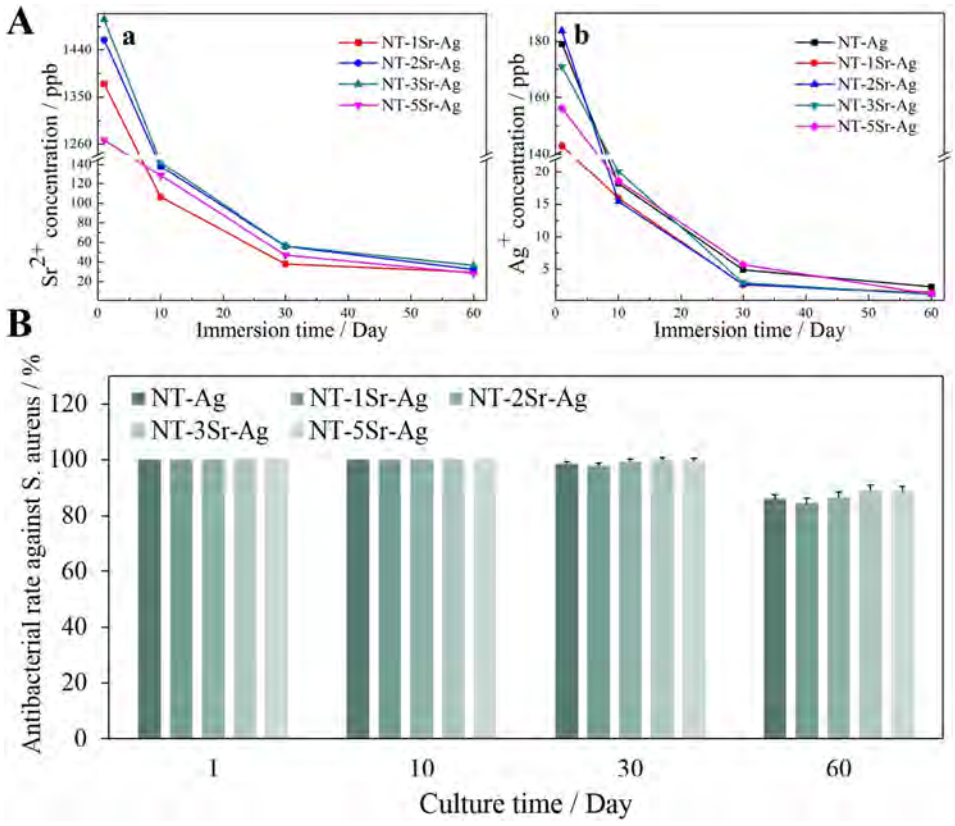

Fig. 3. (A) Non-cumulative release profiles of (a) Sr^{2+} and (b) Ag^{+} from NT-Ag and NT-Sr-Ag; (B) Histograms of the antibacterial rates against *S. aureus*.

correspond to the (110) and (111) planes of cubic crystalline $SrTiO_3$, respectively.

The crystal structure of NT-Ag and NT-Sr-Ag are further investigated by TEM as shown in Fig. 2. The uniform bundle structure of the NTs and slight thickening of the nanotubular wall after HT (NT-Sr-Ags compared with NT-Ag) are disclosed by the low-magnification images (Fig. 2a1–e1) in agreement with SEM. The high-magnification image of NT-Ag in Fig. 2a2 demonstrates that the crystalline NPs are embedded in the amorphous TiO_2 NT walls and the interplanar spacings of 0.246 nm and 0.234 nm match the (002) and (101) crystallographic planes of hexagonal Ag_2O, respectively. The HR-TEM images of NT-Sr-Ag (Fig. 2b2–d2) show two sets of fringe lattices from the rectangular areas. The spacing of 0.246 nm (Fig. 2c4, d5) corresponds to Ag_2O and those of 0.225 nm (Fig. 2c5) and 0.276 nm (Fig. 2b4, c6, d4) match the (111) and (110) planes of $SrTiO_3$, respectively. The SAED patterns (Fig. 2b3–e3) collected from the corresponding region exhibit diffraction rings corresponding to the (102), (110), (200), (211), (204), (302), and (303) planes of hexagonal Ag_2O and (100), (110), (111), (211), (311), (321), and (331) planes of cubic $SrTiO_3$ further confirming the HR-TEM, XPS, and XRD results.

3.2. Sr and Ag release

Fig. 3A shows the non-cumulative release kinetics of Sr and Ag from NT-Ag and NT-Sr-Ag during a period of 60 days. The profiles show high release rates in the initial stage (10 days) followed by a steady release during the rest of the time. After immersion for 10 days, there is no significant difference in the amounts of Ag released from NT-Ag and NT-Sr-Ag. The quantities of Sr^{2+} leached from NT-2Sr-Ag and NT-3Sr-Ag are larger than those from NT-1Sr-Ag and NT-5Sr-Ag but the differences among them are quite small.

3.3. Antibacterial assay

The long-lasting and effective antibacterial ability of NT-Ag has been demonstrated by our research group [22]. In this study, NT-Ag and NT-Sr-Ag are immersed in 5 mL of daily refreshed PBS for up to 60 days and the antibacterial activity against *S. aureus* is evaluated (Fig. 3B). After immersion for 1 and 10 days, NT-Ag and NT-Sr-Ag can kill all the introduced bacteria with an antibacterial rate of 100%. A slightly smaller antibacterial rate is observed after 30 days and it remains quite high at 84% even after 60 days. There is no significant difference between NT-Ag and NT-Sr-Ag.

3.4. Cell adhesion, cytoskeleton, and viability

Initial cell adhesion is the key step in subsequent proliferation and differentiation on biomaterials [43]. Fig. 4A and B shows the fluorescence images of the adherent cells with DAPI staining after incubation for 4 h and the quantitative results after 0.5, 1, and 4 h. No appreciable difference in initial cell adhesion can be observed from the groups. The cytoskeleton assembly is visualized by F-actin staining as shown in Fig. 4C. After culturing for 1 h, the osteoblasts cultured on NT-Sr-Ag form the cytoskeleton faster than those on NT-Ag as evidenced by the polygonal cell shape on NT-Sr-Ag compared with the generally spherical shape without obvious F-actin fibers on NT-Ag. After incubation for 24 h, the cells on all the samples spread well showing no appreciable difference among different samples. The Live/Dead staining fluorescence images of the osteoblasts after culturing for 1, 3, and 5 days are displayed in Fig. 4D. No dead cells are observed from any samples and the cell quantity increases with time. Cell proliferation is determined by the MTT assay as shown in Fig. 4E. All the samples support cell proliferation throughout the culture period and there is no significant difference among NT-TiO_2, NT-Ag, and NT-Sr-Ags.

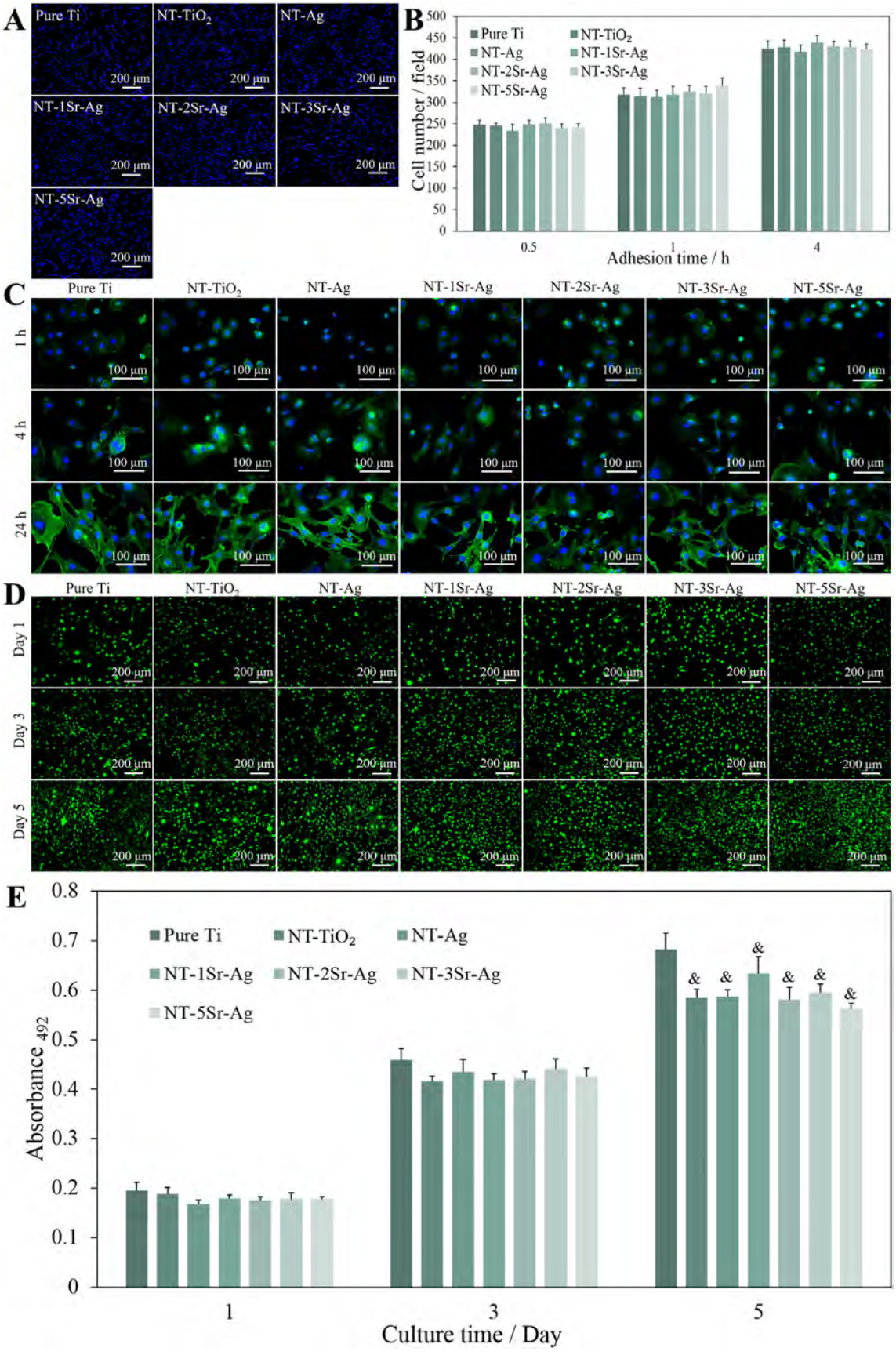

Fig. 4. (A) Fluorescence images of the nuclei of osteoblasts after incubation for 4 h on pure Ti, NT-TiO_2, NT-Ag and NT-Sr-Ag; (B) Quantitative cell adhesion after incubation for 0.5, 1, and 4 h; (C) Fluorescence images of the osteoblasts cultured on the samples with F-actins stained with FITC (green) and nuclei stained with DAPI (blue); (D) Fluorescence images with live/dead staining of the osteoblasts after culturing for 1, 3, and 5 days; (E) MTT results of the osteoblasts after culturing for 1, 3, and 5 days. $^{\&}p < 0.05$ compared to pure Ti. (For interpretation of the references to color in this figure legend, the reader is referred to the web version of this article.)

3.5. Osteogenic differentiation

Osteoblastic differentiation is evaluated by the ALP activity, collagen secretion, and extracellular matrix mineralization of the osteoblasts. The qualitative and quantitative ALP activity after osteogenic induction for 3 and 7 days is shown in Fig. 5A and D, respectively and qualitative ALP staining indexed by the insoluble deep blue NBT-formazan is shown in Fig. 5A. The amounts of NBT-formazan on NT-1Sr-Ag are obviously higher than those on NT-Ag after 3 and 7 days and NT-2Sr-Ag performs better at day 7. ALP production increases with prolonged osteogenic induction and the quantitative ALP activity in Fig. 5D is in good agreement with the qualitative results.

Fig. 5B and E shows the collagen stained by Direct Red 80 together with the quantitative results revealing that no significant difference among all of the nanotubular samples and is more than that on pure Ti after osteogenic induction for 7 days. After 14 days, the collagen on pure Ti and NT-5Sr-Ag is less than that on other samples. The results of extracellular matrix mineralization are shown in Fig. 5C and F. At day 14, matrix mineralization is higher on NT-2Sr-Ag and NT-3Sr-Ag than other samples. After 21 days, NT-Sr-Ag performs better than pure Ti, NT-TiO_2, and NT-Ag.

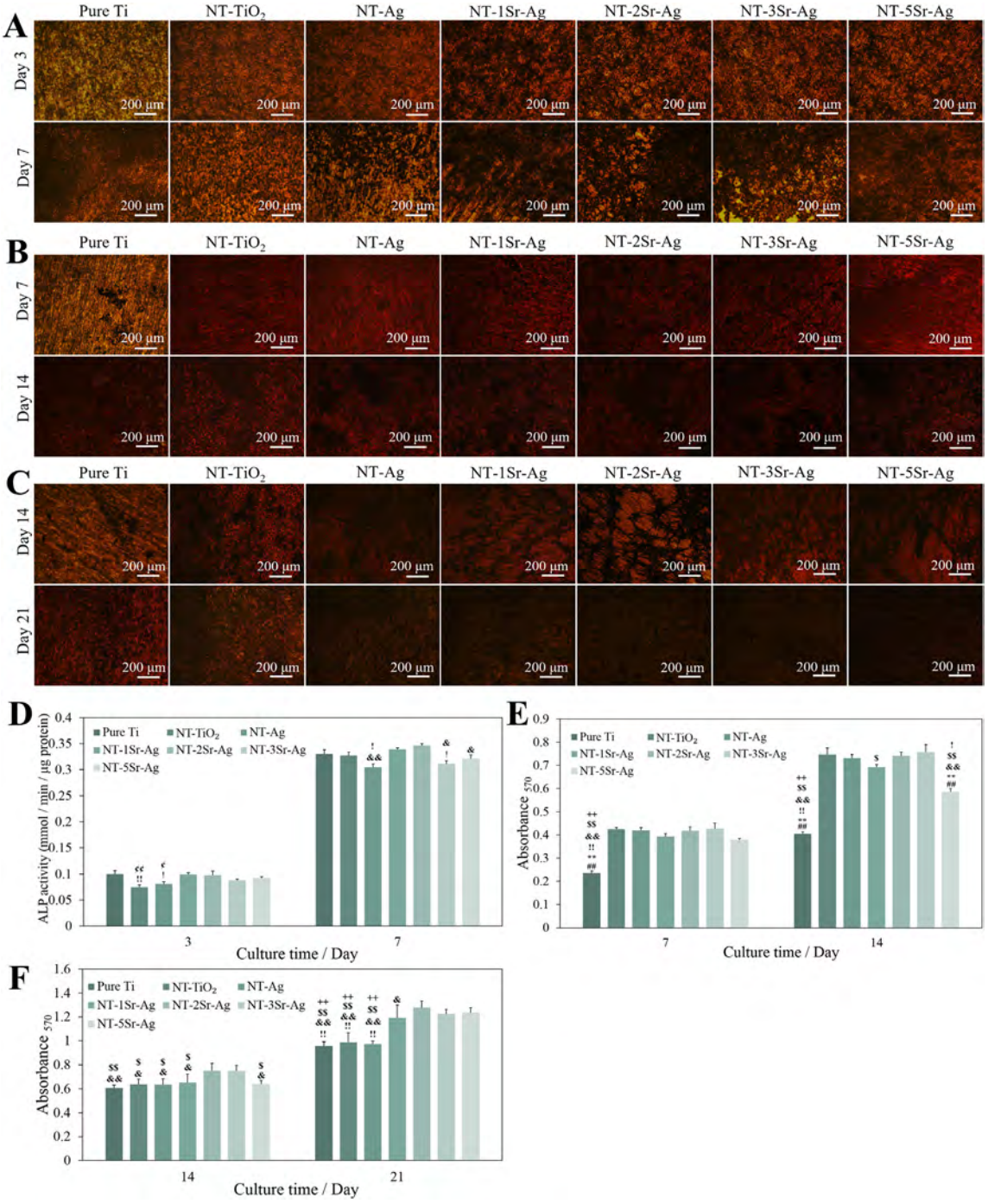

Fig. 5. Qualitative images (A) and quantitative results (D) of ALP activity of the osteoblasts after osteogenic induction for 3 and 7 days; Qualitative images (B) and quantitative results (E) of collagen secreted by the osteoblasts after osteogenic induction for 7 and 14 days; Qualitative images (C) and quantitative results (F) showing the mineralization level of osteoblasts after osteogenic induction for 14 and 21 days. $^{cc}p < 0.01$ and $^{c}p < 0.05$ compared to Pure Ti, $^{\#\#}p < 0.01$ and $^{\#}p < 0.05$ compared to NT-TiO_2, $^{**}p < 0.01$ and $^{*}p < 0.05$ compared to NT-Ag, $^{!!}p < 0.01$ and $^{!}p < 0.05$ compared to NT-1Sr-Ag, $^{\&\&}p < 0.01$ and $^{\&}p < 0.05$ compared to NT-2Sr-Ag, $^{\$\$}p < 0.01$ and $^{\$}p < 0.05$ compared to NT-3Sr-Ag, $^{++}p < 0.01$ compared to NT-5Sr-Ag.

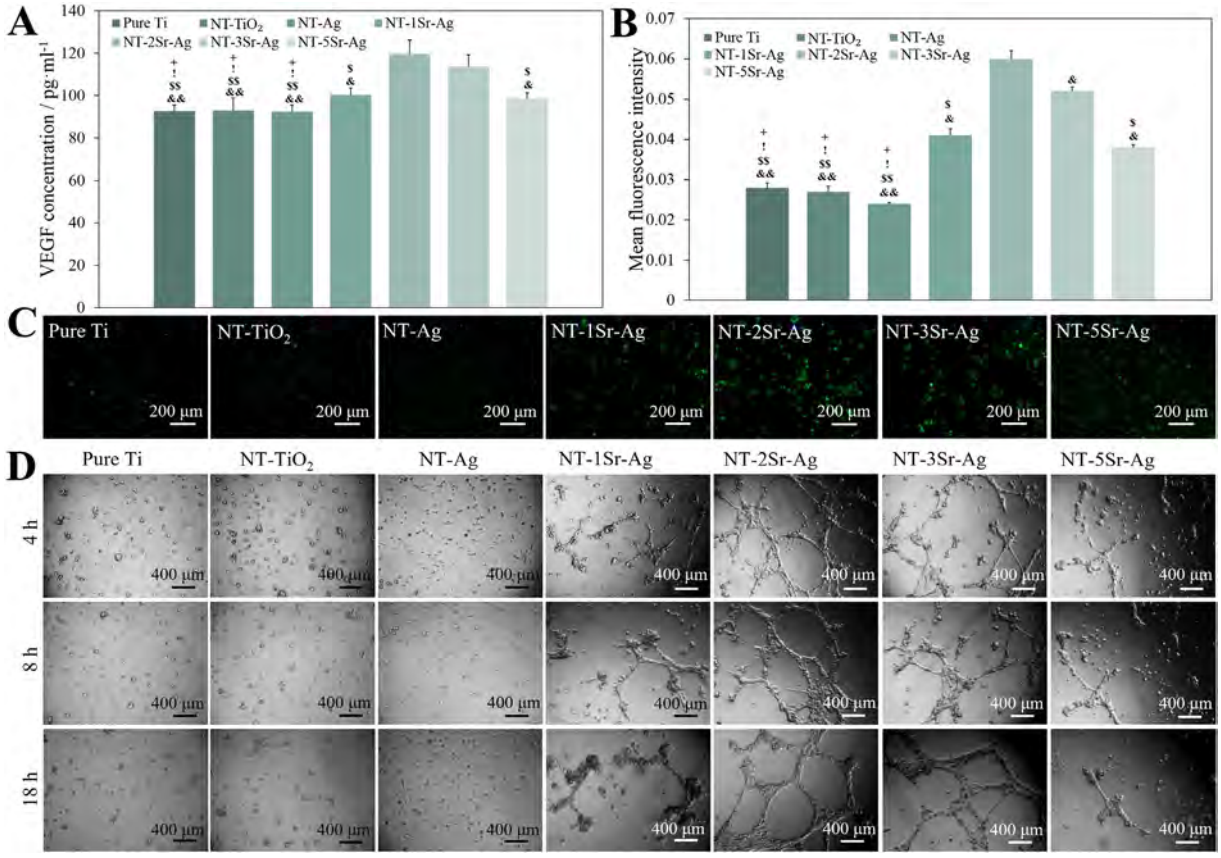

Fig. 6. (A) Quantitative results of VEGF secreted into the supernatant of the culture medium (SCM) obtained from the culture medium of the osteoblasts seeded at a density of 2×10^4 cells/cm^2 and cultured for 48 h; (B) Mean fluorescence intensity of NO production in the ECs stained by the DAF FM-DA fluorescence probe after culturing in SCM for 24 h; (C) Fluorescence images of NO produced by the ECs cultured in SCM for 24 h (B); (D) Optical images of the ECs cultured in SCM on the EC matrix for 4, 8, and 18 h.

3.6. In vitro angiogenesis

The VEGF secreted by the osteoblasts in the SCM is determined by ELISA. As shown in Fig. 6A, NT-Sr-Ag promotes VEGF secretion better than others and better VEGF secretion is induced by NT-2Sr-Ag and NT-3Sr-Ag. The influence of VEGF from the SCM on NO production from ECs is assessed by the NO-sensitive fluorescence probe, DAF-FM DA. The intensity of green fluorescence indicates the level of NO production. Fig. 6C shows that NO fluorescence induced by VEGF in the SCM from NT-Sr-Ag is more intense than that from other groups. The quantitative assessment of the fluorescence intensity in Fig. 6B indicates more NO production by VEGF in the SCM in NT-2Sr-Ag and NT-3Sr-Ag.

The *in vitro* angiogenesis assay kit containing ECMatrix gel is utilized to evaluate the angiogenic ability of ECs cultured with the SCM and the optical images are presented in Fig. 6D. After incubation for 4 h, the ECs cultured with the SCM from NT-Sr-Ag begin to align forming short lines and some branch nodes. After 8 h, the branch nodes and tubes become larger and thicker and bigger ones are observed after 18 h. However, none of such mesh-like structures can be observed from the other groups. In particular, the ECs cultured with the SCM from NT-2Sr-Ag and NT-3Sr-Ag show the best angiogenic activity.

4. Discussion

NT-Sr-Ag is fabricated by HT of NT-Ag which is produced by anodization of deposited TiAg coatings. Under optimal conditions, NT-Sr-Ag shows comparable antibacterial ability and better osteogenic and angiogenic activities than NT-Ag. After the HT, the ordered nanotubular architecture is retained although the tube diameter decreases slightly with HT time due to the volume expansion stemming from the conversion of amorphous TiO_2 to cubic $SrTiO_3$. The hydrothermal reaction takes place on the entire anodized NT walls and the Sr content decreases gradually with depth. This phenomenon can be attributed to the insufficient hydrothermal reaction at deeper sites where cannot be accessed readily by the reactants (*e.g.* Sr^{2+}, OH^-) by diffusion [17]. During HT, some of the Ag_2O nanoparticles are retained and embedded in the NT walls but some go into the solution producing a small Ag concentration of NT-Sr-Ag compared to NT-Ag.

Implants are vulnerable to bacterial infection because of the compromised host defense locally [44,45] endowing implants with long-term antibacterial ability is actively pursued [5]. In our previous study, NT-Ag showed controlled release of Ag^+ to produce excellent antibacterial ability [22]. Here, NT-Sr-Ag produces long-term antibacterial effects comparable to NT-Ag arising from similar Ag release, although the Ag content diminishes after HT. The long-term bacterial resistance demonstrated here is believed to be effective in preventing implant-associated infection for a fairly long period.

Good osteogenic ability is critical in clinical applications. The positive role of Sr in promoting osteogenesis has been demonstrated *in vitro* and *in vivo* [28,46–49]. Although introduction of Sr has little influence on the adhesion, spreading, and proliferation of osteoblasts on NT-Sr-Ag compared to NT-Ag, the former promotes the ALP activity and extracellular matrix mineralization of osteoblasts due to the released Sr^{2+}. Sr^{2+} directly promotes osteoblast functions *via* a calcium sensing receptor dependent mechanism [28–31] and also up-regulates the secretion of VEGF [36,37]. It has been reported that VEGF can stimulate ALP expression and mineralization of osteoblasts but has no appreciable influence on proliferation [38,50] as consistent with our results. Additionally, all the nanotubular samples have more collagen secretion than pure Ti, and the positive effects arising from the nanotubular architecture has been proposed [51].

VEGF not only regulates osteoblast functions, but also acts as a key mediator in angiogenesis. VEGF is a significant bioactive factor in stimulating blood vessel formation by promoting the expression of proangiogenic cytokine receptors [40]. Besides, VEGF initiates the synthesis and production of NO after activating VEGFR-2 [52] and accordingly, the better angiogenic ability of NT-2Sr-Ag and NT-3Sr-Ag may be attributed to the release of more Sr^{2+} which can stimulate osteoblasts to secrete more VEGF [36,37]. On the one hand, good vascular networks can provide the necessary oxygen and nutrients to facilitate cell growth and differentiation to promote implant osseointegration [32, 53,54]. On the other hand, the abundant new vessels also improve the anti-infective ability by delivering host immune cells and molecules to the interface of the bone/implant [35].

5. Conclusion

NT-Sr-Ag that constantly releases Sr^{2+} and Ag^{+} are fabricated hydrothermally from NT-Ag. The hydrothermal treatment does not alter the morphology of the NTs but converts the amorphous TiO_2 in NT-Ag into cubic $SrTiO_3$. During the process, Ag_2O NPs are embedded into the structure. NT-Sr-Ag possesses long-lasting antibacterial activity against *Staphylococcus aureus* because of sustained release of Ag^{+}. NT-Sr-Ag also exhibit good osteogenic and angiogenic activities due to long-term and controllable Sr^{2+} release. NT-2Sr-Ag and NT-3Sr-Ag show good antibacterial, osteogenic, and angiogenic activities and have clinical potential in hard tissue implants.

Acknowledgements

This work was jointly supported by the National Natural Science Foundation of China (31400815, 51671140), Scientific and Technological Innovation Programs of Higher Education Institutions in Shanxi (201626), Hong Kong Research Grants Council (RGC) General Research Funds (GRF) No. CityU 11301215, and City University of Hong Kong Strategic Research Grant (SRG) No. 7004644.

References

[1] Y.F. Feng, L. Wang, Y. Zhang, X. Li, Z.S. Ma, J.W. Zou, W. Lei, Z.Y. Zhang, Biomaterials 34 (2013) 2234–2243.
[2] C. Larsson, P. Thomsen, B.O. Aronsson, P. Tengvall, M. Rodahl, J. Lausmaa, B. Kasemo, L.E. Ericson, Int. J. Biomater. 2013 (2013) 412482.
[3] G.E. Salvi, D.D. Bosshardt, N.P. Lang, I. Abrahamsson, T. Berglundh, J. Lindhe, S. Ivanovski, N. Donos, Periodontol. 68 (2015) 135–152.
[4] D.D. Bosshardt, V. Chappuis, D. Buser, Periodontol. 73 (2017) 22–40.
[5] C.R. Arciola, D. Campoccia, P. Speziale, L. Montanaro, J.W. Costerton, Biomaterials 33 (2012) 5967–5982.
[6] Z. Liu, Y. Zhu, X. Liu, K.W.K. Yeung, S. Wu, Colloids Surf., B 151 (2017) 165–177.
[7] W. Zimmerli, J. Intern. Med. 276 (2014) 111–119.
[8] T. Zhou, Y. Zhu, X. Li, X. Liu, K.W.K. Yeung, S. Wu, X. Wang, Z. Cui, X. Yang, P.K. Chu, Prog. Mater. Sci. 83 (2016) 191–235.
[9] X. Liu, P.K. Chu, C. Ding, Mater. Sci. Eng. R 70 (2010) 275–302.
[10] L. Bai, R. Hang, A. Gao, X. Zhang, X. Huang, Y. Wang, B. Tang, L. Zhao, P.K. Chu, Appl. Surf. Sci. 355 (2015) 32–44.
[11] C.C. Torresa, C.H. Camposa, C. Diáza, V.A. Jiménezb, F. Vidalc, L. Guzmánc, J.B. Alderete, Mater. Sci. Eng. C 65 (2016) 164–171.
[12] P. Roy, S. Berger, P. Schmuki, Angew. Chem. Int. Ed. 50 (2011) 2904–2939.
[13] L. Min, Z. Jin, Z. Su, Mater. Sci. Eng. C 73 (2017) 490–497.
[14] N. Wang, H. Li, W. Lü, J. Li, J. Wang, Z. Zhang, Y. Liu, Biomaterials 32 (2011) 6900–6911.
[15] L. Zhao, L. Liu, Z. Wu, Y. Zhang, P.K. Chu, Biomaterials 33 (2012) 2629–2641.
[16] T. Wang, Z. Weng, X. Liu, K.W.K. Yeung, H. Pan, S. Wu, Bioact. Mater. (2017) http://dx.doi.org/10.1016/j.bioactmat.2017.02.001.
[17] Y. Xin, J. Jiang, K. Huo, T. Hu, P.K. Chu, ACS Nano 3 (2009) 3228–3234.
[18] Y. Zhu, X. Liu, K.W.K. Yeung, P.K. Chu, S. Wu, Appl. Surf. Sci. 400 (2017) 14–23.
[19] L. Zhao, H. Wang, K. Huo, X. Zhang, W. Wang, Y. Zhang, Z. Wu, P.K. Chu, Biomaterials 34 (2013) 19–29.
[20] L. Bai, R. Wu, Y. Wang, X. Wang, X. Zhang, X. Huang, L. Qin, R. Hang, L. Zhao, B. Tang, J. Mater. Chem. B 4 (2016) 5548–5559.
[21] Z. Chen, D. Yi, X. Zheng, J. Chang, C. Wu, Y. Xiao, J. Mater. Chem. B 2 (2014) 6030–6043.
[22] A. Gao, R. Hang, X. Huang, L. Zhao, X. Zhang, L. Wang, B. Tang, S. Ma, P.K. Chu, Biomaterials 35 (2014) 4223–4235.
[23] M. Li, X. Liu, Z. Xu, K.W.K. Yeung, S. Wu, ACS Appl. Mater. Interfaces 8 (2016) 33972–33981.
[24] R. Hang, A. Gao, X. Huang, X. Wang, X. Zhang, L. Qin, B. Tang, J. Biomed. Mater. Res. A 102 (2014) 1850–1858.
[25] M. Zong, L. Bai, Y. Liu, X. Wang, X. Zhang, X. Huang, R. Hang, B. Tang, Mater. Sci. Eng. C 71 (2017) 93–99.
[26] J. Li, D. Zhai, F. Lv, Q. Yu, H. Ma, J. Yin, Z. Yi, M. Liu, J. Chang, C. Wu, Acta Biomater. 36 (2016) 254–266.
[27] W. Zhang, Y. Shen, H. Pan, K. Lin, X. Liu, B.W. Darvell, W.W. Lu, J. Chang, L. Deng, D. Wang, W. Huang, Acta Biomater. 7 (2011) 800–808.
[28] E. Bonnelye, A. Chabadel, F. Saltel, P. Jurdic, Bone 42 (2008) 129–138.
[29] J. Coulombe, H. Faure, B. Robin, M. Ruat, Biochem. Bioph. Res. Co. 323 (2004) 1184–1190.
[30] C. Capuccini, P. Torricelli, F. Sima, E. Boanini, C. Ristoscu, B. Bracci, G. Socol, M. Fini, I.N. Mihailescu, A. Bigi, Acta Biomater. 4 (2008) 1885–1893.
[31] J. Braux, F. Velard, C. Guillaume, S. Bouthors, E. Jallot, J.M. Nedelec, D. Laurent-Maquin, P. Laquerriere, Acta Biomater. 7 (2011) 2593–2603.
[32] P. Carmeliet, J. Intern. Med. 255 (2004) 538–561.
[33] R.A.D. Carano, E.H. Filvaroff, Drug Discov. Today 8 (2003) 980–989.
[34] A.L. Raines, R. Olivares-Navarrete, M. Wieland, D.L. Cochran, Z. Schwartz, B.D. Boyan, Biomaterials 31 (2010) 4909–4917.
[35] X. Hu, K.G. Neoh, Z. Shi, E.T. Kang, C. Poh, W. Wang, Biomaterials 31 (2010) 8854–8863.
[36] F. Liu, X. Zhang, X. Yu, Y. Xu, T. Feng, D. Ren, J. Mater. Sci. Mater. Med. 22 (2011) 683–692.
[37] K. Lin, P. Liu, L. Wei, Z. Zou, W. Zhang, Y. Qian, Y. Shen, J. Chang, Chem. Eng. J. 222 (2013) 49–59.
[38] V. Midy, J. Plouet, Biochem. Bioph. Res. Co. 199 (1994) 380–386.
[39] M.O. Hiltunen, M. Ruuskanen, J. Huuskonen, A.J. Mähönen, M. Ahonen, J. Rutanen, V.M. Kosma, A. Mahonen, H. Kröger, S. Ylä-Herttuala, FASEB J. 17 (2003) 1147–1149.
[40] N. Ferrara, H.P. Gerber, J. LeCouter, Nat. Med. 9 (2003) 669–676.
[41] J. Ng, S. Xu, X. Zhang, H.Y. Yang, D.D. Sun, Adv. Funct. Mater. 20 (2010) 4287–4294.
[42] X. Zhang, K. Huo, L. Hu, Z. Wu, P.K. Chu, J. Am. Ceram. Soc. 93 (2010) 2771–2778.
[43] K. Anselme, Biomaterials 21 (2000) 667–681.
[44] L.G. Harris, S. Tosatti, M. Wieland, M. Textor, R.G. Richards, Biomaterials 25 (2004) 4135–4148.
[45] P.H. Chua, K.G. Neoh, E.T. Kang, W. Wang, Biomaterials 29 (2008) 1412–1421.
[46] M. Hott, P. Deloffre, Y. Tsouderos, P.J. Marie, Bone 33 (2003) 115–123.
[47] M. Shahnazari, N.A. Sharkey, G.J. Fosmire, R.M. Leach, J. Bone Miner. Res. 21 (2006) 1696–1703.
[48] H. Zhu, D. Zhai, C. Lin, Y. Zhang, Z. Huan, J. Chang, C. Wu, J. Mater. Chem. B 4 (2016) 6200–6212.
[49] K. Lin, L. Xia, H. Li, X. Jiang, H. Pan, Y. Xu, W.W. Lu, Z. Zhang, J. Chang, Biomaterials 34 (2013) 10028–10042.
[50] H. Mayer, H. Bertram, W. Lindenmaier, T. Korff, H. Weber, H. Weich, J. Cell. Biochem. 95 (2005) 827–839.
[51] L. Zhao, S. Mei, P.K. Chu, Y. Zhang, Z. Wu, Biomaterials 31 (2010) 5072–5082.
[52] H. Li, K. Xue, N. Kong, K. Liu, J. Chang, Biomaterials 35 (2014) 3803–3818.
[53] P. Carmeliet, Nature 438 (2005) 932–936.
[54] D.H.R. Kempen, L. Lu, A. Heijink, T.E. Hefferan, L.B. Creemers, A. Maran, M.J. Yaszemski, W.J.A. Dhert, Biomaterials 30 (2009) 2816–2825.